

Quantum nuclear motion in silicene: Assessing structural and vibrational properties through path-integral simulations

Carlos P. Herrero and Miguel del Canizo

Instituto de Ciencia de Materiales de Madrid, Consejo Superior de Investigaciones Científicas (CSIC), Campus de Cantoblanco, 28049 Madrid, Spain

(Dated: September 30, 2024)

This paper explores the interplay between quantum nuclear motion and anharmonicity, which causes nontrivial effects on the structural and dynamical characteristics of silicene, a two-dimensional (2D) allotrope of silicon with interesting electronic and mechanical properties. Employing path-integral molecular dynamics (PIMD) simulations, we investigate the quantum delocalization of nuclei, unraveling its impact on the behavior of silicene at the atomic scale. Our study reveals that this delocalization induces significant deviations in the structural parameters of silicene, influencing in-plane surface area, bond lengths, angles, compressibility, and overall lattice dynamics. Through extensive simulations, we delve into the temperature-dependent behavior between 25 and 1200 K, unveiling the role of quantum nuclear fluctuations in dictating thermal expansion and phonon spectra. The extent of nuclear quantum effects is assessed by comparing results of PIMD simulations using an efficient tight-binding Hamiltonian, with those obtained from classical molecular dynamics simulations. The observed quantum effects showcase non-negligible deviations from classical predictions, emphasizing the need for accurate quantum treatments in understanding the material's behavior at finite temperatures. At low T , the 2D compression modulus of silicene decreases by a 14% due to quantum nuclear motion. We compare the magnitude of quantum effects in this material with those in other related 2D crystalline solids, such as graphene and SiC monolayers.

Keywords: Silicene, molecular dynamics, quantum effects

I. INTRODUCTION

Silicene, a two-dimensional allotrope of silicon, has garnered significant attention due to its relevant properties and potential applications across diverse fields. Serving as the silicon counterpart to graphene, silicene boasts advantages rooted in its atomic structure and electronic properties [1–8]. Its intrinsic semiconducting nature and compatibility with existing silicon-based technology position it as a promising candidate for next-generation electronics. With remarkably high electronic mobility and a tunable bandgap, silicene paves the way for efficient and high-speed transistors, enhancing the capabilities of integrated circuits. Beyond electronics, silicene's versatility shines through. Its flexibility, interaction with light, and compatibility with various substrates facilitate applications in sensing, photonics, and nanoelectromechanical systems [4, 9–14]. This breadth of potential applications underscores the importance of further exploration into silicene's properties and functionalities.

From a theoretical standpoint, silicene has been investigated using *ab-initio* density-functional theory (DFT) calculations, which have provided reliable insights into its properties [7, 15, 16]. Unlike graphene's planar structure, these calculations reveal that silicene tends to adopt a buckled configuration, indicating a competition between sp^2 and sp^3 electronic hybridization, with the former prevailing in graphene [7, 15, 16]. DFT-based analyses have been instrumental in examining various aspects of silicene's behavior. They have shed light on its bending characteristics [17–19], mechanical properties [20–23], phonon behavior [24–26], and thermal conductivity [27–

29]. Moreover, DFT calculations have extended to the study of silicene multilayers, elucidating the evolution of physical properties from single-layer configurations to bulk silicon [30–33].

Finite-temperature atomistic simulations, notably molecular dynamics, have been utilized by diverse research teams to examine the mechanical and thermal characteristics of both free-standing and supported silicene, operating within both equilibrium and nonequilibrium scenarios. These simulations often relied on effective potentials such as Tersoff, Stillinger-Weber, and modified embedded atom methods [34–43]. The breadth of these investigations encompasses a wide range of silicene properties, including tensile strength, bending behavior, oscillatory dynamics, and equilibrium responses under various loading conditions. Moreover, researchers have scrutinized the effects of vacancies, the evolution of fracture, and thermal conductivity, frequently drawing comparisons with graphene for a comprehensive understanding of silicene's characteristics [34–43].

Despite the wealth of dependable insights offered by classical molecular dynamics (MD) simulations, the intrinsic quantum nature of silicon nuclei introduces potential discrepancies in calculated physical properties, particularly at temperatures below the Debye temperature of silicene, Θ_D . The range of estimates for Θ_D falls between 550 and 680 K [26, 33, 42], notably surpassing typical room temperatures. To reconcile this quantum aspect, the Feynman path-integral method emerges as a suitable approach, leveraging MD or Monte Carlo sampling techniques [44–47]. By employing the path-integral procedure, the nuclear degrees of freedom can be

effectively quantized, thus accommodating thermal and quantum fluctuations at finite temperatures. This framework facilitates quantitative analyses of anharmonic effects in condensed matter, particularly in the realm of two-dimensional (2D) materials. In this regard, investigations into quantum nuclear motion have unveiled significant impacts on the structural and thermodynamic properties of various 2D materials, including graphene [48, 49], as well as monolayers of SiC and BN [50, 51].

In the low-temperature limit, graphene and 2D SiC exhibit quantum nuclear motion, resulting in zero-point energies of 172 and 86 meV/atom, respectively. For these layered materials, nuclear quantum effects significantly impact the interatomic distances, layer areas, and thermodynamic properties at low temperatures, and can even be noticeable at room temperature [48–50]. In the paradigmatic case of graphene, zero-point expansion due to quantum nuclear motion leads to an approximate 1% increase in the in-plane area. Additionally, the temperature dependence of the in-plane area can vary qualitatively when derived from classical versus path-integral molecular dynamics (PIMD) simulations, even at temperatures between $T = 300$ and 1000 K [48, 49]. At low temperatures, PIMD simulations reveal that the specific heat for stress-free graphene changes as $c_p \sim T$, transitioning to a $c_p \sim T^2$ dependence under tensile stress [52]. Such quantum simulations have also been utilized to study isotopic effects in this material [53]. For 2D layers of SiC, the bending constant and 2D modulus of compression are lower than those of graphene. This indicates that SiC is more susceptible to in-plane stresses. Consequently, nuclear quantum motion, combined with anharmonicity of vibrational modes, produces more directly observable effects in SiC layers.

For silicene, a deep understanding of its structural, mechanical, and thermodynamic properties is essential for an accurate characterization, especially considering its potential technological applications. These properties are expected to be influenced by the quantum motion of silicon nuclei, similar to graphene and SiC layers. However, a key difference between silicene and these other 2D materials is its lack of strict planarity, which may significantly affect the elastic and electronic properties. Consequently, the coupling of electronic and nuclear degrees of freedom (i.e., electron-phonon interaction) in the presence of competing sp^2 and sp^3 hybridizations is likely crucial for an accurate characterization of silicene at finite temperatures.

In this paper, we present the outcomes of comprehensive PIMD simulations conducted on silicene layers. By leveraging this theoretical framework, we embark on a quantitative exploration of thermal and quantum nuclear fluctuations spanning a wide range of temperatures. Our objective is to furnish an in-depth analysis, informed by analogous research on other 2D materials, thereby offering both qualitative and quantitative insights that significantly enrich our comprehension of these systems.

In our study, we delve into the influence of quantum

nuclear motion on both the structural and vibrational characteristics of silicene, contrasting these effects with the expected behavior under classical motion (i.e., classical dynamics of the Si atoms). Our simulations employ interatomic interactions derived from an effective tight-binding (TB) Hamiltonian calibrated to DFT-derived data. We scrutinize the impact of anharmonicity on the physical attributes of silicene by juxtaposing our simulation outcomes with those obtained from a harmonic approximation for the vibrational modes. The realm of path-integral simulations concerning Si-containing materials has seen prior exploration, primarily focusing on aspects such as atomic quantum delocalization and anharmonic effects [50, 54].

The paper is structured as follows. In Sec. II, we detail the computational methodologies underpinning our calculations, encompassing the tight-binding method and PIMD. Sec. III elaborates on the harmonic approximation used for studying the vibrational density of states, important for analyzing anharmonicities in silicene. Moving to Sec. IV, we delve into an analysis of the internal energy, dissecting its kinetic and potential components. Sec. V is dedicated to examining structural properties, including interatomic distance, Si-Si-Si angle, and in-plane area. Sec. VI offers insights into the 2D modulus of compression at various temperatures. Finally, the main results are summarized in Sec. VII.

II. SIMULATION METHOD

Molecular dynamics and Monte Carlo simulations, employing the Feynman path-integral formulation of quantum statistical mechanics, stand as pivotal tools for analyzing many-body systems at finite temperatures. Among these techniques, PIMD simulations are renowned for their adeptness in capturing quantum phenomena inherent in atomic nuclei behavior. This methodology hinges on an isomorphism which equates a quantum system to a virtual classical one. In this approach, each quantum particle, such as a Si nucleus in our context, is symbolized by a ring polymer comprising N_{Tr} (Trotter Number) beads interconnected by harmonic strings [44, 45, 47]. Through this association, the partition function of the quantum system assumes a structure reminiscent of a classical system. In this framework, an effective potential emerges from the harmonic interactions among neighboring beads within each of the N (number of particles) polymer rings. The formal exactitude of the partition function is attained for $N_{\text{Tr}} \rightarrow \infty$. Additional insights into this computational method can be found elsewhere [45–47, 55].

In our simulations of silicene, the dynamics of atomic nuclei are governed by a Born-Oppenheimer energy surface derived from an effective non-orthogonal tight-binding Hamiltonian [56–58], constructed via DFT calculations. This Hamiltonian emerges as a balance between accuracy, transferability, and computational effi-

ciency. The approach presented by Porezag et al. [56] operates on the basis of the linear combination of atomic orbitals (LCAO) method within the local density approximation (LDA). It involves the creation of a pseudo-atom endowed with a collective confinement potential derived from the covalent radius of the target atom. The eigenfunctions of this pseudo-atom serve as the basis for a minimal orbital set, where the wavefunctions of the extended system are expressed through an LCAO equation. The computation of Hamiltonian and overlap matrices within the LDA employs a two-center approximation and Slater-Koster integrals. This hybrid *ab initio*-parameterized TB methodology harnesses appropriate input densities and potentials, without the need for experimental data adjustments. Such a TB model, characterized by its integration of *ab initio* calculations with parameterized elements, has found prior application in studies concerning silicon [59–62] and Si-containing materials [50, 57, 63, 64]. Other TB parameterizations have been also employed to study several properties of silicon by MD simulations, including defect diffusion and phase transformations [65–67].

We performed PIMD simulations on silicene layers within the isothermal-isobaric ensemble, keeping the number of particles (N), temperature (T), and in-plane stress (τ) constant. The stress, measured as force per unit length, corresponds to what is referred to in the literature as mechanical or frame tension [68–70]. The bead coordinates within the ring polymers were represented using staging variables. We integrated the equations of motion, specifically adapted for 2D materials, using reversible integrators with factorization techniques for the Liouville time-evolution operator. In particular, we utilized the reversible system propagator algorithm (RESPA) [71, 72]. This approach allowed for the adaptive use of distinct time steps: $\Delta t = 1$ fs for dynamical variables associated with interatomic forces, and $\delta t = 0.25$ fs for faster dynamical variables involving harmonic bead interactions and thermostats.

Temperature control was achieved by coupling a chain of four Nosé-Hoover thermostats, with a “mass” parameter $Q = \beta\hbar^2/5N_{\text{Tr}}$, to each staging variable ($\beta = 1/k_B T$ and k_B is Boltzmann’s constant). Consequently, each of the $3N$ atomic momentum coordinates was coupled to a separate chain of M thermostats. This extensive thermostating of the system is essential in PIMD simulations to prevent the emergence of ergodicity issues. In classical MD simulations, it would also be appropriate to use a single thermostat chain for all atoms. The primary reason for employing massive thermostating in our calculations is that the additional computational cost is minimal, allowing the same computational code to be used for both PIMD and classical MD simulations.

To maintain a constant in-plane stress ($\tau = 0$ in this case), we coupled the xy surface area of the simulation cell to a barostat with an effective “mass” W (with dimensions of energy \times time²), which is further connected to a chain of M thermostats [46, 73]. Specifically, for the

time derivative of the in-plane area of the simulation cell, $A = NA_p$, the equation $dA/dt = 2Ap_A/W$ was applied, where p_A is an effective “momentum” associated with A , having dimensions of energy \times time. In this work, we set $M = 4$ and $W = 3.2 \times 10^{15}$ eV fs², following Ref. [72]. We verified that this choice of parameters is sufficient for ensuring controlled system equilibration, as well as for maintaining the desired temperature and external stress. In particular, using $M = 4$ ensures rapid equilibration, and no significant change was observed with larger values of M .

The dynamical equations in the $N\tau T$ ensemble involve the time derivatives of the position and momentum coordinates of the dynamic degrees of freedom in the extended system, which includes staging modes, chains of Nosé-Hoover thermostats, the volume, and the barostat [46, 73]. The thermostats and barostat introduce friction terms into the dynamical equations, resulting in non-Hamiltonian dynamics. However, it is possible to define a quantity analogous to the total energy in the extended system, which is conserved during the dynamical process. This conserved quantity serves as a useful check for the accuracy of the numerical integration of the equations of motion (see, e.g., Ref. [73]). To calculate the kinetic energy E_{kin} , we used the virial estimator. This method is particularly advantageous due to its lower statistical uncertainty compared to that of the potential energy, especially at high temperatures [73, 74].

The choice of N_{Tr} in PIMD simulations is influenced by two main considerations. Firstly, it is important to ensure consistent accuracy across the entire temperature range. To achieve this, we scale the Trotter number according to the relationship $N_{\text{Tr}}T = 6000$ K, following earlier guidelines outlined in Refs. [48, 75]. At room temperature ($T = 300$ K), this corresponds to ring polymers with 20 beads. Secondly, a finite N_{Tr} introduces a cutoff frequency, which in our case is $\omega_c = N_{\text{Tr}}k_B T/\hbar \approx 4200$ cm⁻¹. This frequency significantly exceeds the vibrational frequencies observed in silicene. Thus, the highest frequency of optical phonons is $\omega_m \approx 680$ cm⁻¹, resulting in $\omega_c/\omega_m \approx 6$. This ratio ensures good convergence of vibrational properties with respect to the Trotter number in our quantum simulations. We verified this convergence at $T = 300$ K by considering values of N_{Tr} up to 60, and found that the results for the variables studied here were consistent within statistical error bars when compared to $N_{\text{Tr}} = 20$. Specifically, the energy differences were smaller than 1 meV/atom. With our choice of N_{Tr} for each temperature T , the imaginary time step between successive beads in the ring polymers is given by $\beta\hbar/N_{\text{Tr}} = 1.3$ fs, which is comparable to the time step used for integrating the dynamical equations in our PIMD simulations ($\Delta t = 1$ fs, see above).

We used rectangular simulation cells with similar side lengths in the x and y directions of the xy reference plane, applying periodic boundary conditions. Silicon atoms were allowed unrestricted movement in the out-of-plane direction, implementing free boundary conditions along

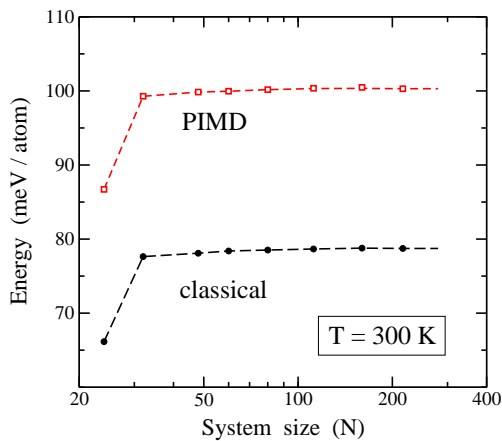


FIG. 1: System size dependence of the energy for silicene at $T = 300$ K, computed using the TB Hamiltonian presented in this study. Circles represent results from classical MD, while open squares depict outcomes from PIMD simulations. Lines are guides to the eye. Energy values are referenced to the minimum-energy state for a system size $N = 216$.

the z axis to model a free-standing silicene layer. We verified that isotropic changes in cell dimensions during $N\tau T$ simulations yielded the same results for the studied variables as using flexible cells, which allow independent changes in the x and y axis lengths, along with deformations of the rectangular shape. Additionally, to assess the impact of boundary conditions, we utilized supercells of the primitive hexagonal cell and observed no changes in our results.

In our simulations, we considered silicene supercells containing $N = 60, 112,$ and 216 atoms. To efficiently sample the electronic degrees of freedom in reciprocal space, we focused solely on the Γ point ($\mathbf{k} = 0$). While considering larger \mathbf{k} sets may induce slight changes in total energy, these variations are negligible for the energy differences pertinent to our discussion. We have observed that any shift in the minimum energy E_0 becomes increasingly inconsequential with larger cell sizes. Sampling the configuration space encompassed temperatures ranging from 25 to 1200 K. Typical simulation protocols involved 2×10^5 PIMD steps for system equilibration, followed by 8×10^6 steps for computing average properties. We have checked that this simulation length is much larger than the autocorrelation time Ω of the variables studied in this paper, for our zero-stress conditions. In particular, Ω for the in-plane area A_p appreciably increases as the system size rises, and for the largest size considered here, we have found autocorrelation times shorter than 10^5 simulation steps.

To gauge the significance of quantum effects elucidated by our PIMD simulations, we conducted classical MD simulations using the same TB Hamiltonian. In this scenario, $N_{\text{Tr}} = 1$, resulting in the collapse of ring polymers into single beads. This approach allows for a direct comparison between quantum and classical data, shedding

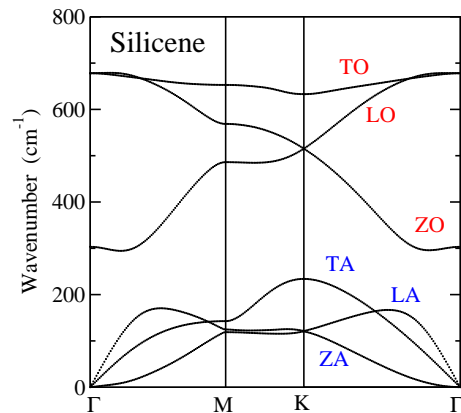


FIG. 2: Phonon dispersion branches of silicene, $\omega_j(\mathbf{k})$, found from diagonalization of the dynamical matrix for the TB Hamiltonian used in this work. Labels indicate the six phonon bands.

light on the extent to which quantum fluctuations influence the behavior of the system.

In Fig. 1, we depict the size dependency of the energy derived from our simulations of silicene conducted at $T = 300$ K. Circles represent data from classical MD simulations, while open squares denote results obtained from PIMD simulations. Across both datasets, we observe a slow increase in energy for $N > 30$. Energy changes for varying system sizes remain below 2 meV for $N > 50$, and decrease to less than 1 meV for $N > 100$. It is worth noting that the disparity between the two datasets remains constant at 22 meV/atom for $N > 30$.

Furthermore, to contextualize our findings concerning buckled silicene, the predicted configuration for this 2D material, we conducted classical MD simulations of planar silicene, characterized by a strictly flat configuration. This planar structure has been previously scrutinized by several researchers employing diverse theoretical methodologies [3, 4, 15, 30, 42, 76, 77]. Comparing results for both buckled and planar silicene offers insights into the energetics and dynamics of this material, enriching our understanding of its fundamental properties.

III. HARMONIC APPROXIMATION

In evaluating the significance of anharmonicity in our PIMD simulations for silicene, we adopt a harmonic approximation (HA) for the vibrational modes. In this method, frequencies are derived for the minimum-energy configuration and are assumed to remain constant, irrespective of temperature. Similarly, the in-plane area, A_p , is treated as constant, thereby disregarding thermal fluctuations, as well as thermal expansion or contraction. While the HA typically provides reliable estimates at low temperatures in solids, its accuracy diminishes as temperature increases due to the growing influence of an-

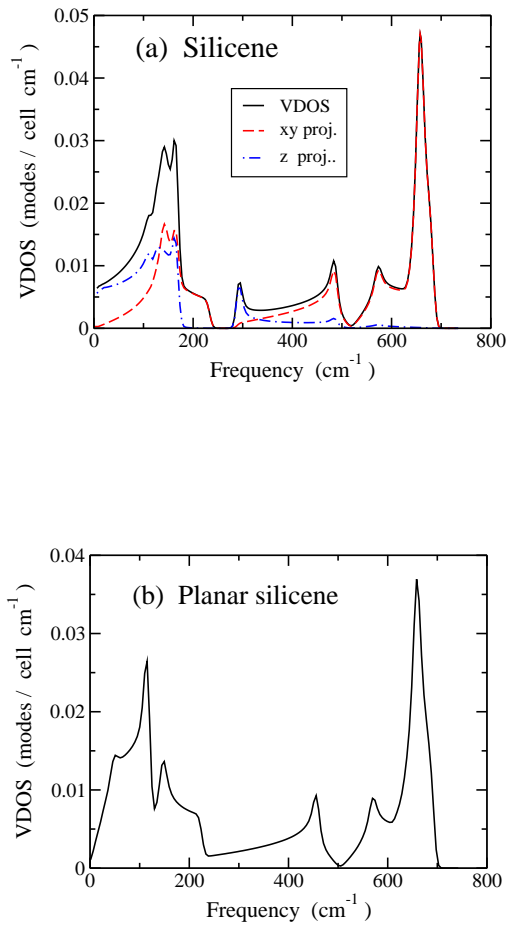


FIG. 3: (a) Vibrational density of states of silicene, obtained in the HA for the TB Hamiltonian used in this paper (solid line). Dashed and dashed-dotted lines indicate the in-plane (xy) and out-of-plane (z) projections of the VDOS, respectively. (b) VDOS for planar silicene (only xy component).

harmonicity. Consequently, one anticipates an increasing disparity between the predictions of the HA and the more accurate simulation results as temperature rises.

In Fig. 2, we illustrate the phonon bands of silicene along symmetry directions within the 2D hexagonal Brillouin zone, as determined in the HA through the diagonalization of the dynamical matrix, employing the TB Hamiltonian. Labels denote the six phonon branches depicted in the plot. The phonon dispersion showcased in Fig. 2 is similar to those observed in studies utilizing empirical potentials [78] and DFT calculations [23–26, 29, 77]. Notably, we observe the presence of the flexural ZA band, characteristic of 2D materials.

To directly quantify the overall anharmonicity, we computed the vibrational density of states (VDOS), $\rho(\omega)$, across the entire Brillouin zone. Employing numerical integration, we followed the methodology outlined in Ref. [79]. Fig. 3(a) illustrates the resulting VDOS for silicene, depicted by a solid line.

For a more thorough analysis, we computed the pro-

jection of the eigenvectors resulting from the diagonalization of the dynamical matrix onto the in-plane x , y , and out-of-plane z directions, thereby determining their respective contributions to the VDOS using the expression [80]:

$$\rho^j(\omega, \hat{\mathbf{n}}) = \frac{1}{N} \sum_{\lambda} \delta(\omega - \omega_{\lambda}) |\hat{\mathbf{n}} \cdot \mathbf{e}_{\lambda}^j|^2, \quad (1)$$

where j denotes the atoms within the crystallographic unit cell (here, $j = 1, 2$), $\hat{\mathbf{n}}$ represents a unit projection vector, λ iterates over the frequency eigenvalues, and \mathbf{e}_{λ}^j signifies the eigenvector of mode λ . Subsequently, for a given direction, let us say x , the VDOS along that direction is given by $\rho_x(\omega) = \rho^1(\omega, \hat{\mathbf{n}}_x) + \rho^2(\omega, \hat{\mathbf{n}}_x)$.

In Fig. 3(a), we have plotted the projected VDOS along the z direction (dashed-dotted line), as well as the projection onto the layer plane encompassing the x and y directions (dashed line). The predominant contribution of the z component is evident for frequencies below 200 cm^{-1} , corresponding to acoustic modes.

Our calculations on silicene employing the TB Hamiltonian reveal a distinct gap in the VDOS between 240 and 280 cm^{-1} , delineating the frequency regimes of acoustic and optical modes. This stands in contrast to graphene, where such a gap is absent [81–84], and its presence in silicene can be attributed to the lack of planarity. To elucidate this disparity, we computed the VDOS for planar silicene, as depicted in Fig. 3(b). Since planar silicene does not represent the energetically favorable configuration under the employed TB Hamiltonian, computing vibrational modes in three-dimensional space results in unphysical imaginary frequencies for out-of-plane (z direction) vibrations. Therefore, the VDOS shown in Fig. 3(b) captures the dynamics of strictly planar silicene in 2D space, encompassing only in-plane vibrations. Above 300 cm^{-1} , this VDOS closely resembles that of buckled silicene, as depicted in Fig. 3(a), since in this frequency range it is predominantly influenced by projections in the xy plane. Notably, the gap observed between 240 and 280 cm^{-1} in the buckled material is absent in the planar counterpart.

IV. ENERGY

In this section, we examine the evolution of silicene’s energy with respect to temperature, as derived from our PIMD simulations. We juxtapose these findings with results from classical MD simulations and the HA, aiming to discern the effects of quantum nuclear motion and anharmonicity of the atomic vibrations.

In Fig. 4(a), we present the temperature-dependent energy, $E - E_0$, extracted from PIMD simulations (open squares), where E_0 denotes the energy of the minimum-energy configuration. This configuration corresponds to the classical zero-temperature limit, devoid of quantum delocalization effects. For comparison, the results ob-

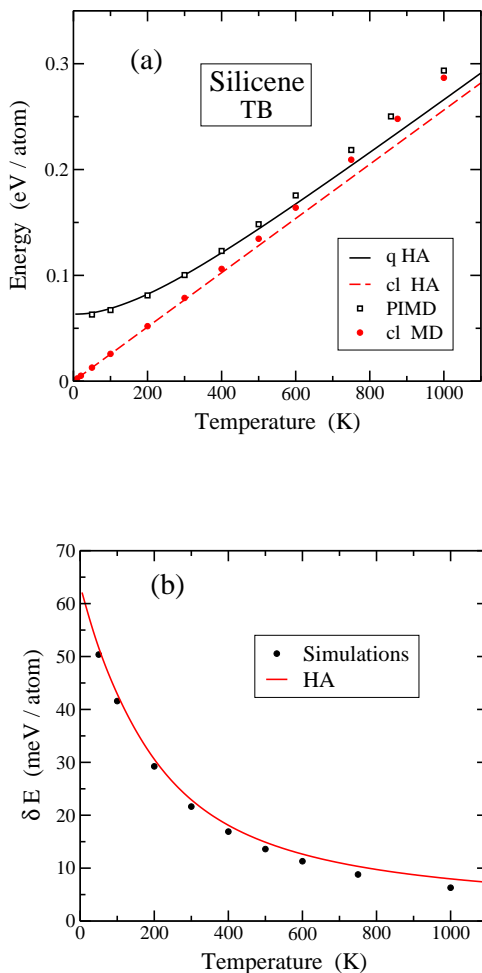


FIG. 4: (a) Energy as a function of temperature. Symbols indicate results of simulations using the TB Hamiltonian: classical MD (circles) and PIMD (open squares). The solid line is the vibrational energy derived from the VDOS shown in Fig. 3(a). The dashed line indicates the classical vibrational energy in a harmonic approximation: $E_{\text{vib}}^{\text{cl}} = 3k_B T$. (b) Difference δE between quantum and classical results. Solid circles, data derived from simulations; continuous line, harmonic approximation.

tained from classical MD simulations are depicted as circles. At low temperatures, the quantum data converge to a zero-point energy, $E_{\text{ZP}} = 62$ meV/atom. Converted to a mean frequency, $\bar{\omega}$, using the relationship $E_{\text{ZP}} = \hbar\bar{\omega}/2$, this yields $\bar{\omega} = 333$ cm^{-1} . Remarkably, this value closely aligns with the average frequency derived from the VDOS showcased in Fig. 3(a), which amounts to $\bar{\omega} = 340$ cm^{-1} .

For comparison with the simulation data, we present results of the HA in both classical (dashed line) and quantum (solid line) scenarios. At temperature T , the quantum-mechanical vibrational energy per atom, E_{vib} , within the HA framework is determined from the VDOS

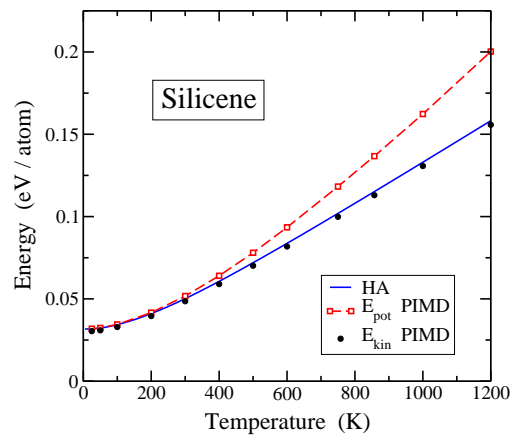


FIG. 5: Temperature dependence of the kinetic (solid circles) and potential energy (open squares), derived from PIMD simulations. The solid line represents the kinetic and potential energy derived from the HA. The dashed curve is a guide to the eye.

$\rho(\omega)$ through a continuous approximation, given by:

$$E_{\text{vib}} = \frac{1}{4} \int_0^{\omega_m} \hbar \omega \coth\left(\frac{1}{2}\beta\hbar\omega\right) \rho(\omega) d\omega, \quad (2)$$

where $\beta = 1/k_B T$ and ω_m denotes the maximum frequency in the phonon spectrum. To account for the six degrees of freedom in a crystallographic unit cell (comprising two Si atoms), we ensure the normalization condition:

$$\int_0^{\omega_m} \rho(\omega) d\omega = 6. \quad (3)$$

At low temperatures, the classical simulation data closely adhere to the harmonic approximation ($E = E_0 + 3k_B T$), with both datasets exhibiting deviations from each other for $T > 400$ K. This deviation progressively increases to reach 12% (30 meV/atom) at $T = 1000$ K. We note that the departure of the classical energy from the harmonic expectation is solely attributed to the potential energy. In this scenario, the kinetic energy per atom remains constant, given by $E_{\text{kin}} = 3k_B T/2$, regardless of anharmonicity. The divergence between the PIMD results and the quantum HA becomes noticeable at approximately the same temperature of 400 K. By $T = 1000$ K, this deviation reaches 10% (27 meV/atom), after which classical and quantum simulation results demonstrate convergence with increasing temperature.

The discrepancy between quantum and classical outcomes for the energy, δE , spanning from $T = 0$ to 1000 K, is depicted in Fig. 4(b). This plot illustrates the data obtained from our simulations (circles), alongside the energy difference derived from the HA (solid line). At low temperatures, the difference δE derived from the simulations appears marginally smaller than the discrepancy inferred from the HA. However, as the temperature escalates, this disparity gradually expands.

A criterion for gauging the extent of overall anharmonicity lies in comparing the kinetic and potential energies, which are separately provided by PIMD simulations. In the realm of harmonic vibrations, both energies coincide at all temperatures, as dictated by the virial theorem, irrespective of the underlying approach, classical or quantum. Fig. 5 illustrates the kinetic and potential energies derived from PIMD simulations as a function of temperature: E_{pot} (depicted by open squares) and E_{kin} (represented by circles). The solid curve portrays the outcome of the HA, derived from the VDOS using Eq. (2), where both energies align. The dashed line serves as a visual guide for the potential energy. For temperatures below 400 K, the potential energy closely mirrors the kinetic energy, while the former escalates more rapidly than the latter at higher T . Anharmonicities in the interatomic potential lead to a notable increase in E_{pot} with temperature, while the kinetic energy remains closely aligned with the harmonic approximation. At $T = 1000$ K, the difference $E_{\text{pot}} - E_{\text{kin}}$ amounts to 24% of the kinetic energy.

Our findings contribute to a deeper understanding of electron-phonon interactions in silicene, moving beyond the limitations of harmonic or quasi-harmonic approximations for lattice vibrational modes. Such interactions can alter the electronic structure of 2D materials, in a manner similar to what has been observed in crystalline solids like diamond or cubic SiC [64, 85]. In these materials, nuclear quantum motion and anharmonic effects, particularly at low temperatures, lead to a renormalization (reduction) of the electronic band gap. For example, the direct gap at the Γ point decreases by approximately 10% as $T \rightarrow 0$. In silicene, the electronic gap can be modulated through various methods, including the application of perpendicular electric fields, chemical functionalization (e.g., hydrogenation, oxidation), metal atom adsorption, or by using confined structures [6]. A precise understanding of the electronic structure and its modifications due to electron-phonon interactions is critical for potential applications of silicene in electronic devices. As in three-dimensional (3D) materials, the actual electronic gap in buckled silicene is expected to be influenced by nuclear quantum motion. This can result in changes of up to 10% in the gap, a significant shift that would notably affect the electrical conductivity and other electronic properties. Further exploration of this subject is needed, both experimentally and theoretically, particularly through future studies utilizing PIMD simulations.

V. STRUCTURAL PROPERTIES

A. Interatomic distance

In the pursuit of the minimum-energy configuration of silicene at the classical zero temperature limit, the TB Hamiltonian reveals a distinctive buckled chair-like structure, characterized by an interatomic distance of

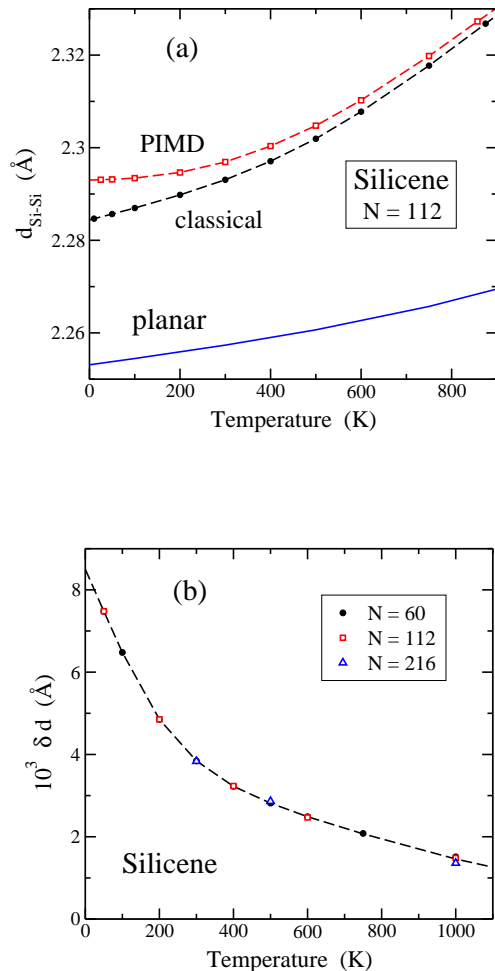


FIG. 6: (a) Temperature dependence of the mean distance between nearest-neighbor atoms in silicene, derived from classical (solid circles) and PIMD simulations (open squares) for $N = 112$. Error bars are smaller than the symbol size. The solid line represents the interatomic distance obtained from classical MD simulations of planar silicene. (b) Difference δd between quantum and classical results for $N = 60$ (circles), 112 (squares), and 216 (triangles). Dashed lines in (a) and (b) are guides to the eye.

$d_{\text{Si-Si}} = 2.284$ Å. The vertical displacement (z coordinate) between adjacent silicon atoms, amounts to $h = 0.574$ Å. This structural feature emerges from the interplay between sp^2 and sp^3 hybridization, the latter being characteristic of bulk silicon with tetrahedral coordination of Si atoms. Several DFT calculations corroborate the non-planar nature of silicene, predicting an out-of-plane buckling distance h ranging between 0.44 and 0.49 Å [15, 76, 77, 86, 87], along with a separation between nearest neighbors, $d_{\text{Si-Si}}$, varying from 2.24 to 2.28 Å [15, 76, 77, 86].

In the case of planar silicene (buckling distance $h = 0$), our investigation reveals a minimum-energy configuration with an interatomic distance of $d_{\text{Si-Si}} = 2.253$ Å, marginally shorter than the buckled counterpart. This

flat configuration exhibits an energy 86 meV/atom higher than the absolute minimum, E_0 . Such a difference forms a substantial energy barrier, effectively favoring the buckled structure. It is noteworthy that at room temperature ($T = 300$ K), the thermal energy per degree of freedom (e.g., along the z coordinate) amounts to $k_B T = 26$ meV/atom. This comparison underscores the energetic preference for buckled silicene, emphasizing the persistence of its structural stability even under thermal agitation.

Turning to the outcomes of our simulations at finite temperatures, Fig. 6(a) illustrates the distance $d_{\text{Si-Si}}$ across the temperature range from $T = 0$ to 900 K. The data points, represented by solid circles and open squares, correspond to classical MD and PIMD simulations, respectively, both conducted with a system size of $N = 112$. Remarkably, the influence stemming from the finite cell size remains small compared to the statistical error bars, a consistent observation across both classical and quantum results (further discussed below).

In the classical approach, our findings confirm the expected linear relationship that characterizes bond expansion in crystalline solids at low temperatures [88]. This linear trend holds up to approximately $T = 200$ K, with our results yielding a slope of $\partial d_{\text{Si-Si}}/\partial T = 2.7 \times 10^{-5}$ Å/K within this temperature range. However, beyond this threshold, significant deviations from linearity become apparent. For example, at $T = 875$ K, the extrapolated Si-Si bond distance from the low-temperature linear fit, $d_{\text{Si-Si}} = 2.308$ Å, contrasts with the actual value from MD simulations, $d_{\text{Si-Si}} = 2.327$ Å, indicating a relative increase of 0.8%. This nonlinearity is more pronounced compared to similar materials such as 2D SiC [50] or graphene [48], largely due to silicene's distinct buckled structure, which amplifies bond dilation with rising temperatures. At 875 K, classical simulations for graphene and SiC monolayers show a relative difference of less than 0.1% between the simulation results at this temperature and the linear extrapolation of the interatomic distance from low-temperature data. This underscores the significantly enhanced anharmonicity observed in buckled silicene compared to planar materials.

To obtain deeper insight into this departure from linearity, we carried out classical simulations for planar silicene at various temperatures, while maintaining the z coordinate of silicon atoms fixed at $z = 0$. The outcomes of these simulations, portraying the interatomic distance as a function of T , are depicted in Fig. 6(a) by a solid line. For $T \rightarrow 0$, $d_{\text{Si-Si}}$ converges to a value of 2.253 Å, aligning with the previously mentioned minimum-energy configuration for planar silicene. This value is smaller than that observed in unrestricted simulations, where atomic motion is free in the out-of-plane direction. Earlier DFT calculations also corroborate a reduction in the interatomic distance for the planar configuration compared to the buckled minimum-energy structure of silicene. Indeed, reported values of $d_{\text{Si-Si}}$ ranging between 2.22 and 2.25 Å have been documented in such calcula-

tions [77, 86].

Our simulations of planar silicene reveal a noteworthy trend in the relationship between $d_{\text{Si-Si}}$ and T , appearing to approximate linearity across a broader temperature range compared to the buckled material, as illustrated in Fig. 6(a). Specifically, for planar silicene, we observe a slope of $\partial d_{\text{Si-Si}}/\partial T = 1.4 \times 10^{-5}$ Å/K at low temperatures. This value is approximately half of that obtained for the buckled counterpart (as discussed earlier).

The interplay between the anharmonicity inherent in the interatomic potential derived from the TB Hamiltonian and the atomic quantum dynamics is anticipated to induce an expansion in the equilibrium distance $d_{\text{Si-Si}}$. This effect becomes evident through the noticeable gap observed between the curves representing PIMD and classical MD simulations in Fig. 6(a). As $T \rightarrow 0$, extrapolations from PIMD simulations conducted at finite temperatures indicate a Si-Si distance of 2.293 Å, indicative of a bond expansion $\Lambda_0 = 8.5 \times 10^{-3}$ Å, attributed to zero-point motion. The difference between quantum and classical data gradually diminishes with increasing temperature. This reduction in difference can be attributed to the diminishing influence of quantum fluctuations as temperature rises, culminating in the convergence of the two curves at elevated temperatures.

The zero-point expansion Λ_0 found between low-temperature PIMD and classical MD simulation data, amounting to 0.4% of the bond length, can be compared to relative quantum-to-classical expansions reported from similar TB calculations for related materials. Specifically, these expansions are 0.5% in graphene [89] and 0.3% in 2D silicon carbide [50]. The relative values of Λ_0 for the three 2D materials are of the same order of magnitude, despite the large variation in interatomic distances for C-C, C-Si, and Si-Si bonds (1.429, 1.720, and 2.284 Å, respectively). Notably, this relative quantity Λ_0 reaches its minimum value for the binary compound SiC.

In Fig. 6(b), we illustrate the temperature-dependent behavior of the interatomic bond expansion, δd , resulting from quantum motion. This expansion is derived from the difference between the outcomes of PIMD and classical MD simulations at each temperature. Starting from the zero-point value Λ_0 , δd gradually diminishes to 1.5×10^{-3} Å at 1000 K, indicating a reduction by a factor of approximately 6 within this temperature range. At $T = 300$ K, δd measures 3.8×10^{-3} Å, equivalent to 45% of Λ_0 . The plot presents data for system sizes $N = 60$ (depicted by solid circles), 112 (open squares), and 216 (open triangles). For each temperature, the data obtained for different cell sizes coincide within the error bars, and in most instances they appear superimposed in Fig. 6(b).

When examining the buckling distance h , our PIMD simulations reveal a measurement of 0.579 Å at low temperatures, slightly higher than the classical counterpart of 0.574 Å. This increase in h equates to roughly 1% of the classical value. However, with the escalation of temperature, we observe a reduction in the buckling dis-

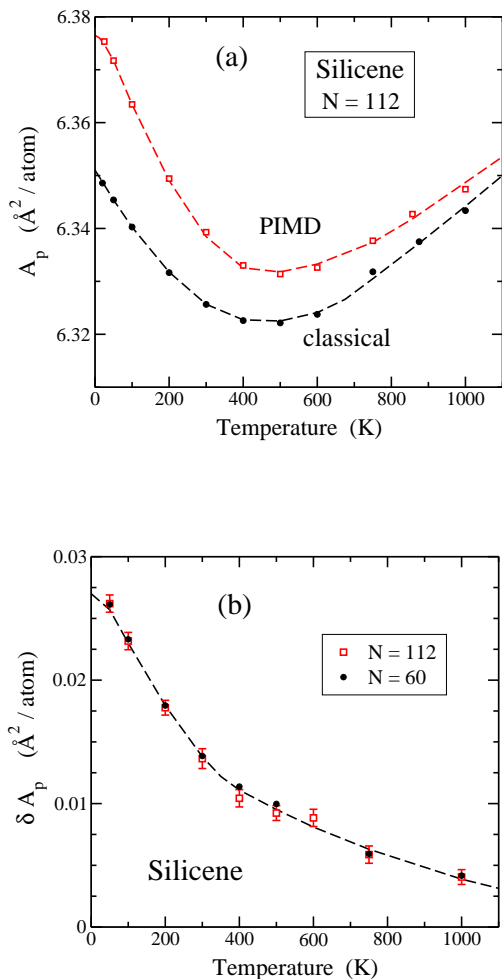


FIG. 7: (a) In-plane area, A_p , as a function of temperature, derived from classical (circles) and PIMD simulations (open squares). Error bars are in the order of the symbol size. (b) Difference, δA_p , between quantum and classical results vs T for $N = 60$ (solid circles) and 112 (open squares). Lines are guides to the eye.

tance, yielding $h = 0.557$ and 0.559 \AA at $T = 1000 \text{ K}$ from classical and quantum simulations, respectively. It is important to emphasize that these data reflect average values computed over long simulation runs. The actual difference in z coordinates between silicon atoms fluctuates notably within each configuration, as does the mean value across various simulation steps, particularly at elevated temperatures. This variability primarily stems from the bending of the silicene layer under thermal agitation.

B. In-plane area

Simulations performed in the isothermal-isobaric ensemble afford three-dimensional freedom to the Si atoms to move in space. This setup allows us to calculate the

in-plane area A_p of silicene and its behavior with respect to temperature. Note that A_p is the conjugate variable to the in-plane stress τ , which we impose to vanish in our simulations.

In Fig. 7(a), we illustrate the in-plane area A_p as a function of temperature, derived from classical MD (circles) and PIMD simulations (open squares). At low temperatures, the classical results converge to the minimum-energy state, characterized by an in-plane area $A_p^0 = 6.351 \text{ \AA}^2/\text{atom}$. The length d_{xy} of a Si-Si bond projection on the xy plane satisfies $d_{xy}^2 = d_{\text{Si-Si}}^2 - h^2$, and $A_p = 3\sqrt{3}d_{xy}^2/4$. Across both types of simulations, the in-plane area A_p decreases in the temperature range from $T = 0$ to 400 K, indicating a contraction with $\partial A_p/\partial T < 0$. In the classical data, a minimum in A_p is evident at a temperature $T_m \approx 450 \text{ K}$, whereas the quantum result exhibits a slightly higher value around 500 K. This trend of T_m increasing when nuclear quantum effects are considered has been previously observed in graphene [48].

The behavior of the in-plane area A_p with temperature is governed by the interplay of two competing factors. Firstly, the atomic motion out of the plane induces a reduction in A_p , a phenomenon linked to the mean-square fluctuation (MSF), $(\Delta z)^2$, at each temperature [90]. Secondly, thermal expansion of the Si-Si bonds results in an enlargement of the crystalline membrane, promoting an increase in the actual in-plane area. At low temperatures, the former effect predominates, leading to a negative rate of change: $\partial A_p/\partial T < 0$. While the MSF $(\Delta z)^2$ does increase with temperature, this increment follows a sublinear trend [90, 91]. In contrast, the elongation of the Si-Si bond length with rising temperature exhibits a superlinear trend (see Fig. 6(a)). Consequently, as temperature increases, the dominance shifts towards the second mechanism, resulting in $\partial A_p/\partial T > 0$.

Furthermore, in Fig. 7(b), we depict the variance between quantum and classical outcomes for $N = 60$ and 112 atoms. The figure notably illustrates the convergence of classical results towards quantum outcomes as temperature rises. The disparity in area between quantum and classical findings diminishes from its zero-point value, $\delta A_p^0 = 2.7 \times 10^{-2} \text{ \AA}^2/\text{atom}$, with increasing temperature. At $T = 1000 \text{ K}$, this difference narrows to $4 \times 10^{-3} \text{ \AA}^2/\text{atom}$, representing a sevenfold reduction in quantum expansion compared to the zero-temperature limit. This consistent trend is observable across different sizes of the simulation cell, as illustrated in Fig. 7(b).

For planar silicene, the area A_p is determined to be $6.595 \text{ \AA}^2/\text{atom}$ for the minimum-energy configuration (classical, $T = 0$). In this scenario a thermal expansion of the 2D material becomes apparent when it is strictly confined to the $z = 0$ plane, contrasting with the reduction of A_p observed for buckled silicene at low temperatures. This difference arises as a direct consequence of the inhibition of bending in the planar configuration. At low temperatures, we observe a positive slope of $\partial A_p/\partial T = 5 \times 10^{-5} \text{ \AA}^2/\text{K}$, a significant departure from

the negative slope of $-1.2 \times 10^{-4} \text{ \AA}^2/\text{K}$ corresponding to classical results for buckled silicene.

We conclude this section by emphasizing the importance of in-plane area variations in ensuring compatibility with other materials in epitaxial structures [4]. Specifically, the increase in A_p due to nuclear quantum motion can impact the functionality of potential devices. Lattice mismatches between adjacent material layers may lead to the formation of misfit dislocations, which can degrade microelectronic device performance by introducing undesirable electrical properties or compromising mechanical stability. Thus, understanding these area changes is crucial for optimizing the functionality of epitaxial structures in practical applications. In the case of silicene, the quantum effects related to in-plane area (or lattice parameters) discussed here can significantly influence its growth and structural properties in epitaxial systems. These effects could be explored on various substrates, such as silver, aluminum, or MoS_2 [92], where small lattice mismatches (on the order of 1% or even less) may play a crucial role in determining the stability and performance of silicene-based structures.

C. Si-Si-Si angle

In bulk silicon, which adopts a face-centered cubic diamond structure, the bond angle between an atom and two of its nearest neighbors is $\phi = 109.47^\circ$, indicative of sp^3 electronic hybridization in Si atoms. Conversely, in a planar 2D atomic layer with a honeycomb structure, such as graphene or strictly flat silicene, the bond angle ϕ is 120° , reflecting sp^2 hybridization. In the case of silicene, which exhibits an actual buckled structure, the bond angle ϕ assumes intermediate values between these two limits due to the interplay between sp^2 and sp^3 hybridization in this material.

The Si-Si-Si angle in silicene is subject to fluctuations due to the combined effects of thermal and quantum motion affecting the silicon atoms. In Fig. 8(a), we illustrate the temperature-dependent variation of the average angle ϕ as determined from classical MD simulations (depicted as solid circles) and PIMD simulations (open squares). Across both simulation methods, one observes that the angle decreases with increasing temperature, exhibiting a tendency to converge towards each other at elevated temperatures. In the $T = 0$ classical limit, we find $\phi = 113.90^\circ$, which notably aligns closer to the angle corresponding to tetrahedral 3D coordination rather than the hexagonal 2D case (the mean value for these two configurations being 114.7°). Upon extrapolating the PIMD simulation results towards zero temperature ($T \rightarrow 0$), the angle ϕ is estimated to be $\phi = 113.76^\circ$, somewhat smaller than the classical minimum.

From a purely geometric perspective, the angle ϕ can be directly correlated with both the interatomic bond length $d_{\text{Si-Si}}$ and the buckling distance h . Specifically, in the absence of atomic motion, as in the classical $T = 0$

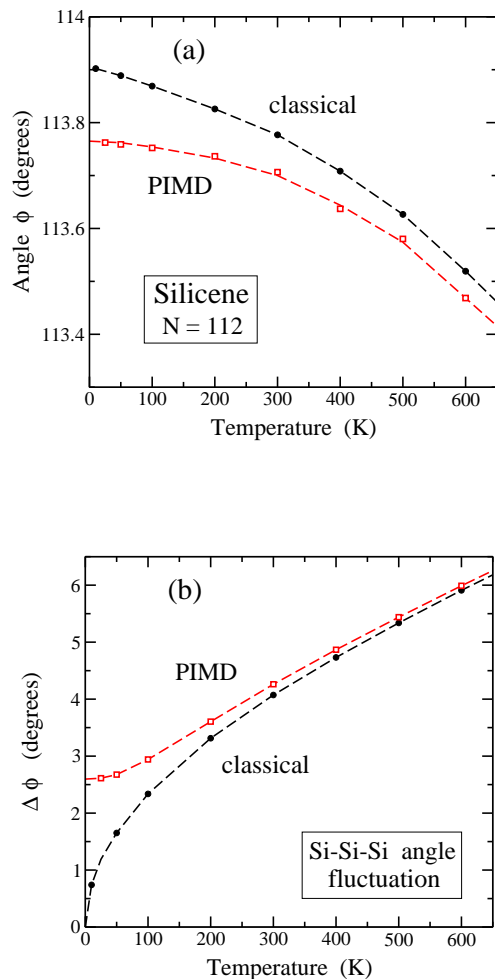


FIG. 8: (a) Temperature dependence of (a) the mean Si-Si-Si angle ϕ in silicene, and (b) its root-mean-square fluctuation $\Delta\phi$. Solid circles and open squares represent results from classical MD and PIMD simulations, respectively. Dashed lines are guides to the eye. Error bars are on the order of the symbol size.

limit, this relationship is succinctly expressed by:

$$\cos \phi = \frac{1}{2}(3c^2 - 1), \quad (4)$$

where $c = h/d_{\text{Si-Si}}$. It is noteworthy that Eq. (4) reproduces the expected angles for distinct structural configurations: for a planar sheet ($c = 0$), it yields $\phi = 120^\circ$, while for the tetrahedral 3D arrangement ($c = 1/3$), it predicts $\cos \phi = -1/3$. However, it is important to acknowledge that in the presence of atomic motion, whether classical thermal or quantum, the accuracy of Eq. (4) diminishes. This is primarily attributed to the induced bending within the silicene layer.

In Fig. 8(b), we illustrate the root-mean-square fluctuation $\Delta\phi$ of the Si-Si-Si angle, as determined from classical MD (depicted as solid circles) and PIMD simulations (open squares). For $T \rightarrow 0$, $\Delta\phi$ converges to zero

for the classical data. Conversely, for the quantum results, a value of 2.6° is observed due to zero-point motion. With increasing temperature, $\Delta\phi$ escalates rapidly. At $T = 1000$ K (not shown in the figure), it reaches approximately 8° for both classical and quantum data. At this temperature, the difference between the two is less than 0.05° .

VI. COMPRESSIBILITY

Mechanical and elastic properties are crucial for understanding the strength, reliability, and design of silicene-based devices. A detailed understanding of the mechanical response provides valuable insights for applications in various systems, including those used in nanoelectronics [20–23]. Additionally, structural changes or deformations can impact the performance of these applications by altering the electronic band structure.

PIMD simulations offer valuable insights into the elastic characteristics of solids, particularly in the realm of 2D crystalline membranes. These properties undergo significant influence from quantum nuclear motion, particularly noticeable at temperatures below the Debye temperature of the materials under investigation.

In this section, we examine the in-plane compressibility of silicene, or its inverse, the 2D modulus of hydrostatic compression B_p . For layered materials, the isothermal B_p at temperature T is defined as [93]:

$$B_p = -A_p \left(\frac{\partial \tau}{\partial A_p} \right)_T. \quad (5)$$

Here, the in-plane biaxial pressure τ and area A_p are variables associated with the layer plane, and in the isothermal-isobaric ensemble they behave as conjugate variables. It is worth noting that B_p is linked to the elastic stiffness constants of silicene, as expressed by: $B_p = (C_{11} + C_{12})/2$ [90, 93].

The modulus B_p can also be determined using the fluctuation formula [52, 94]:

$$B_p = \frac{k_B T A_p}{N(\Delta A_p)^2}, \quad (6)$$

where $(\Delta A_p)^2$ represents the MSF of the area A_p , calculated here from classical and quantum simulations under $\tau = 0$. This expression offers an alternative, feasible approach to compute B_p , circumventing the need for deriving $(\partial A_p / \partial \tau)_T$ through numerical methods, which necessitate additional simulations at pressures near $\tau = 0$. We have verified at several temperatures that both methods produce B_p results consistent within the statistical error bars of the simulations. This validation serves as a valuable consistency check for the numerical techniques employed in this study.

In Fig. 9, we present the modulus B_p of silicene as a function of temperature, derived from our PIMD simulations (open squares) and classical MD (solid circles),

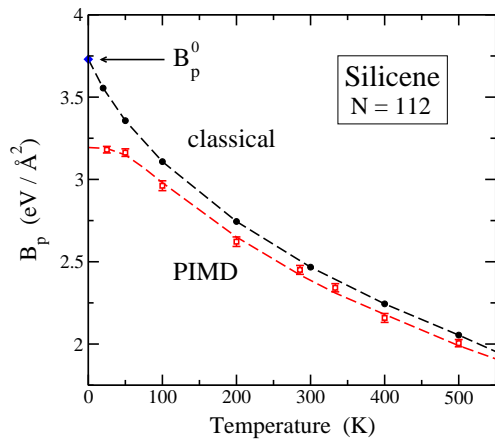


FIG. 9: Two-dimensional modulus of compression B_p of silicene, found from PIMD (open squares) and classical MD simulations (solid circles) for $N = 112$. Error bars of the classical data are on the order of the symbol size. A diamond at $T = 0$, indicated by an arrow, shows the B_p^0 value obtained from Eq. (7) for the minimum-energy configuration. Dashed lines are guides to the eye.

using Eq. (6). The classical 2D modulus B_p , as obtained from our simulations, demonstrates a notable decrease with increasing temperature. Specifically, at low temperatures, we observe a slope of $\partial B_p / \partial T = -7.5 \times 10^{-3}$ eV/(\AA^2 K). However, this slope decreases as the temperature rises, reaching $\partial B_p / \partial T = -1.9 \times 10^{-3}$ eV/(\AA^2 K) at 500 K.

In a classical 2D solid, B_p at $T = 0$ is determined by the expression:

$$B_p^0 = A_p \left. \frac{\partial^2 E}{\partial A_p^2} \right|_{A_p^0}, \quad (7)$$

where E represents the energy. For silicene, B_p^0 is calculated to be 3.73 eV/ \AA^2 , consistent with the extrapolation for $T \rightarrow 0$ of the B_p data derived from our classical simulations. This low-temperature limit of the compression modulus is indicated by an arrow in Fig. 9. As temperature rises, our simulations show decreasing B_p values, as previously noted. For instance, at $T = 750$ K, B_p is determined to be 1.65 eV/ \AA^2 , which represents 44% of the zero-temperature limit, B_p^0 .

For planar silicene, employing Eq. (7), we derive $B_p^0 = 6.2$ eV/ \AA^2 , significantly greater than the equivalent value for the buckled material. This disparity arises because Si–Si bonds in the latter are not aligned parallel to the layer plane, rendering the actual material softer than the ideal planar configuration.

In our quantum results for buckled silicene, shown in Fig. 9 (open squares), we notice a significant decrease in B_p at low temperatures compared to the classical data. Extrapolating the quantum data to $T = 0$ yields $B_p = 3.19$ eV/ \AA^2 , contrasting with the classical low- T value: $B_p^0 = 3.73$ eV/ \AA^2 . This implies a reduction of

14% due to zero-point quantum motion. The disparity between classical and quantum outcomes diminishes with increasing temperature, and at $T = 500$ K it is about 2%.

We highlight that the derivative $\partial B_p / \partial T$ must vanish in the limit $T \rightarrow 0$, in accordance with the third law of Thermodynamics [95, 96]. While this condition is met by PIMD results, classical low-temperature data exhibit a negative slope, violating this principle.

In comparison to the results for silicene, it is worth noting that similar calculations performed for monolayer graphene and 2D SiC yield B_p^0 values of 12.7 and 5.5 eV/Å², respectively [50]. These values, particularly that of graphene, are significantly higher than the corresponding result for silicene. Specifically, the B_p^0 value for graphene is more than three times larger than that of silicene. A substantial portion of this difference arises from the disparity in bond strength, with C–C bonds being considerably stronger than Si–Si bonds. Furthermore, B_p in silicene is further diminished by its nonplanar structure, as previously discussed, with the buckled configuration resulting in a reduction of about 40% compared to the planar form.

In this study, we have shown that nuclear quantum motion in silicene leads to a significant reduction in the 2D compression modulus, particularly at low temperatures, where a decrease of 14% is observed. This reduction can impact the stability of silicene layers in epitaxial structures, where tensile or compressive stresses may arise due to lattice mismatches between different components. At higher temperatures, the average Si–Si bond distance, $d_{\text{Si–Si}}$, increases (see Fig. 6), weakening the bonds and making them more susceptible to breaking under lower levels of tensile strain. Additionally, the Si–Si bond distances exhibit larger fluctuations at elevated temperatures, further contributing to bond breakage.

To conclude this section, it is important to highlight that, although DFT and other computational methods provide reasonable predictions for mechanical properties like the modulus B_p , they usually do not consider the quantum dynamics of atomic nuclei. When this omission is combined with anharmonicity of lattice vibrational modes, significant changes in these properties can arise. This phenomenon affects the modulus B_p , as discussed above, and is also expected to influence the in-plane Young’s modulus E_p . In fact, the latter is related to B_p by the relation $E_p = 2B_p(1 - \nu)$, where ν represents the Poisson’s ratio. Both B_p and E_p are experimentally measurable quantities, and they exhibit nuclear quantum effects, particularly at low temperatures. Comparing computational results with experimental measurements on silicene samples poses a challenge for future research, as significant advancements have been made in recent years, especially in studies involving 2D materials under various conditions. For instance, the mechanical properties of graphene have been investigated using phonon dispersion and low-energy electron diffraction (LEED) techniques on both free-standing and supported samples [97, 98]. Moreover, it is noteworthy that in the

case of silicene, the relative reduction in the modulus B_p due to nuclear quantum motion at low temperatures (14%) is slightly larger than that observed for graphene (12%) in similar PIMD simulations, despite the fact that B_p^0 for silicene is significantly lower than that of graphene. This greater reduction in silicene may enhance the experimental detection of such quantum effects, particularly in the low-temperature regime.

VII. SUMMARY

In this paper, we have shown that PIMD simulations provide a powerful means to assess the impact of nuclear quantum motion on diverse structural and vibrational features of 2D crystalline solids. In the case of silicene, with a Debye temperature around 600 K, we have observed significant nuclear quantum effects even for T exceeding room temperature.

At low temperatures, silicene’s behavior is influenced by a combination of anharmonicity and quantum motion. We have investigated this behavior using a tight-binding Hamiltonian. To gauge the extent of quantum effects, we have compared data from classical MD and PIMD simulations. Additionally, a harmonic approximation serves as a reference point for assessing the magnitude of anharmonicity in various physical properties of silicene.

The quantization of lattice vibrations in silicene induces alterations in the average interatomic distances and in-plane area. The zero-point expansion of A_p corresponds to a 0.4% deviation from the classical calculation, a relative value akin to the bond dilation observed for $T \rightarrow 0$.

The quantum correction to the 2D compression modulus B_p at low temperatures is calculated to be -0.54 eV/Å², equivalent to a 14% reduction from the classical value B_p^0 . This decrease in B_p resulting from nuclear quantum motion underscores the softer nature of real silicene compared to classical predictions, particularly evident at low T .

We highlight the alignment of low-temperature PIMD simulation results with the third law of Thermodynamics. This entails that the temperature derivative of various magnitudes (such as $d_{\text{Si–Si}}$, A_p , B_p) must approach zero as temperature tends to zero. Notably, this feature is absent in classical simulations, a distinction that has not received ample emphasis in the literature about atomistic simulations of materials.

PIMD simulations, similar to those described in this study, have the potential to provide valuable insights into the interplay between anharmonicity and quantization of vibrational modes in stressed silicene. Additionally, they can elucidate similar dynamics in silicene, a hydrogenated silicene layer.

Acknowledgments

We express our gratitude to Rafael Ramírez for his invaluable discussions and assistance with computa-

tional methods. This work was supported by Ministerio de Ciencia e Innovación (Spain) under Grant Number PID2022-139776NB-C66.

-
- [1] H. J. W. Zandvliet, *Nano Today* **9**, 691 (2014).
- [2] L. Tao, E. Cinquanta, D. Chiappe, C. Grazianetti, M. Fanciulli, M. Dubey, A. Molle, and D. Akinwande, *Nature Nanotech.* **10**, 227 (2015).
- [3] C. Grazianetti, E. Cinquanta, and A. Molle, *2D Mater.* **3**, 012001 (2016).
- [4] A. Molle, C. Grazianetti, L. Tao, D. Taneja, M. H. Alam, and D. Akinwande, *Chem. Soc. Rev.* **47**, 6370 (2018).
- [5] J. Zhuang, X. Xu, H. Feng, Z. Li, X. Wang, and Y. Du, *Sci. Bulletin* **60**, 1551 (2015).
- [6] M. A. Kharadi, G. F. A. Malik, F. A. Khanday, K. A. Shah, S. Mittal, and B. K. Kaushik, *ECS J. Solid State Sci. Techn.* **9**, 115031 (2020).
- [7] C. Tantardini, A. G. Kvashnin, C. Gatti, B. Yakobson, I. and X. Gonze, *ACS Nano* **15**, 6861 (2021).
- [8] S. Ghosal, A. Bandyopadhyay, S. Chowdhury, and D. Jana, *Rep. Progr. Phys.* **86**, 096502 (2023).
- [9] Z. Ni, Q. Liu, K. Tang, J. Zheng, J. Zhou, R. Qin, Z. Gao, D. Yu, and J. Lu, *Nano Lett.* **12**, 113 (2012).
- [10] Z.-X. Guo, Y.-Y. Zhang, H. Xiang, X.-G. Gong, and A. Oshiyama, *Phys. Rev. B* **92**, 201413 (2015).
- [11] J. Zhu and U. Schwingenschogl, *2D Mater.* **3**, 035012 (2016).
- [12] H. H. Gurel and B. Salmankurt, *Biosensors* **11**, 59 (2021).
- [13] Q. Guo, J. Liu, C. Bai, N. Chen, and L. Qu, *ACS Nano* **15**, 16533 (2021).
- [14] T.-N. Do, G. Gumbs, P.-H. Shih, D. Huang, C.-W. Chiu, C.-Y. Chen, and M.-F. Lin, *Sci Rep.* **9**, 624 (2019).
- [15] S. Cahangirov, M. Topsakal, E. Akturk, H. Sahin, and S. Ciraci, *Phys. Rev. Lett.* **102**, 236804 (2009).
- [16] S. Trivedi, A. Srivastava, and R. Kurchania, *J. Comp. Theor. Nanosci* **11**, 781 (2014).
- [17] S. Kumar and P. Suryanarayana, *Nanotech.* **31**, 43LT01 (2020).
- [18] A. S. Banerjee and P. Suryanarayana, *J. Mech. Phys. Solids* **96**, 605 (2016).
- [19] M. Pizzochero, M. Bonfanti, and R. Martinazzo, *Phys. Chem. Chem. Phys.* **21**, 26342 (2019).
- [20] H. Zhao, *Phys. Lett. A* **376**, 3546 (2012).
- [21] B. Mortazavi, O. Rahaman, M. Makaremi, A. Dianat, G. Cuniberti, and T. Rabczuk, *Physica E* **87**, 228 (2017).
- [22] S. Yoo, B. Lee, and K. Kang, *Nanotech.* **32**, 295702 (2021).
- [23] J. Zeng, M. Wu, B. Xu, S. Tao, X. Li, and C. Ouyang, *J. Mater. Sci.* **53**, 4306 (2018).
- [24] L.-F. Huang, P.-L. Gong, and Z. Zeng, *Phys. Rev. B* **91**, 205433 (2015).
- [25] J.-A. Yan, R. Stein, D. M. Schaefer, X.-Q. Wang, and M. Y. Chou, *Phys. Rev. B* **88**, 121403 (2013).
- [26] B. Peng, H. Zhang, H. Shao, Y. Xu, G. Ni, R. Zhang, and H. Zhu, *Phys. Rev. B* **94**, 245420 (2016).
- [27] B. Peng, H. Zhang, H. Shao, Y. Xu, R. Zhang, H. Lu, D. W. Zhang, and H. Zhu, *ACS Appl. Mater. Interf.* **8**, 20977 (2016).
- [28] H. Xie, M. Hu, and H. Bao, *Appl. Phys. Lett* **104**, 131906 (2014).
- [29] X. Gu and R. Yang, *J. Appl. Phys.* **117**, 025102 (2015).
- [30] T. Jaroch, M. Krawiec, and R. Zdyb, *2D Mater.* **8**, 035038 (2021).
- [31] J. E. Padilha and R. B. Pontes, *J. Phys. Chem. C* **119**, 3818 (2015).
- [32] B. Ipaves, J. F. Justo, and L. V. C. Assali, *Phys. Chem. Chem. Phys.* **24**, 8705 (2022).
- [33] K. Yang, S. Cahangirov, A. Cantarero, A. Rubio, and R. D'Agosta, *Phys. Rev. B* **89**, 125403 (2014).
- [34] G. R. Berdiyrov and F. M. Peeters, *RSC Adv.* **4**, 1133 (2014).
- [35] D. K. Das and J. Sarkar, *J. Appl. Phys.* **123**, 044304 (2018).
- [36] M. Hu, X. Zhang, and D. Poulikakos, *Phys. Rev. B* **87**, 195417 (2013).
- [37] A. Ince and S. Erkoç, *Comp. Mater Sci.* **50**, 865 (2011).
- [38] N. T. Long, T. Q. Tuan, D. N. A. Thuy, Q. D. Ho, and H. A. Huy, *Molec. Simul.* **49**, 655 (2023).
- [39] T. K. Min, T. L. Yoon, and T. L. Lim, *Mater. Res. Express* **5**, 065054 (2018).
- [40] Q.-X. Pei, Z.-D. Sha, Y.-Y. Zhang, and Y.-W. Zhang, *J. Appl. Phys.* **115**, 023519 (2014).
- [41] S. Rouhi, H. Pourmirzaagha, and A. Farzin, *Mater. Res. Express* **6**, 085004 (2019).
- [42] Z. Wang, T. Feng, and X. Ruan, *J. Appl. Phys.* **117**, 084317 (2015).
- [43] S. Rouhi, *Comp. Mater. Sci.* **131**, 275 (2017).
- [44] R. P. Feynman, *Statistical Mechanics* (Addison-Wesley, New York, 1972).
- [45] M. J. Gillan, *Phil. Mag. A* **58**, 257 (1988).
- [46] C. P. Herrero and R. Ramírez, *J. Phys.: Condens. Matter* **26**, 233201 (2014).
- [47] D. M. Ceperley, *Rev. Mod. Phys.* **67**, 279 (1995).
- [48] C. P. Herrero and R. Ramírez, *J. Chem. Phys.* **145**, 224701 (2016).
- [49] B. G. A. Brito, L. Candido, G. Q. Hai, and F. M. Peeters, *Phys. Rev. B* **92**, 195416 (2015).
- [50] J. C. Noya and R. Ramírez, *J. Phys. Chem. Solids* **171**, 110980 (2022).
- [51] B. G. A. Brito, L. Candido, J. N. Teixeira Rabelo, and G. Q. Hai, *Comp. Condens. Matter* **31**, e00660 (2022).
- [52] C. P. Herrero and R. Ramírez, *Phys. Rev. B* **97**, 195433 (2018).
- [53] C. P. Herrero and R. Ramírez, *Eur. Phys. J. B* **93**, 146 (2020).
- [54] J. C. Noya, C. P. Herrero, and R. Ramírez, *Phys. Rev. B* **53**, 9869 (1996).
- [55] C. Cazorla and J. Boronat, *Rev. Mod. Phys.* **89**, 035003 (2017).
- [56] D. Porezag, T. Frauenheim, T. Köhler, G. Seifert, and R. Kaschner, *Phys. Rev. B* **51**, 12947 (1995).
- [57] R. Gutierrez, T. Frauenheim, T. Köhler, and G. Seifert, *J. Mater. Chem.* **6**, 1657 (1996).
- [58] C. M. Goringe, D. R. Bowler, and E. Hernández, *Rep.*

- Prog. Phys. **60**, 1447 (1997).
- [59] T. Frauenheim, F. Weich, T. Kohler, S. Uhlmann, D. Porezag, and G. Seifert, Phys. Rev. B **52**, 11492 (1995).
- [60] P. Klein, H. M. Urbassek, and T. Frauenheim, Comp. Mater. Sci. **13**, 252 (1999).
- [61] P. Klein, H. M. Urbassek, and T. Frauenheim, Phys. Rev. B **60**, 5478 (1999).
- [62] M. Kaczmariski, O. N. Bedoya-Martinez, and E. R. Hernandez, Phys. Rev. Lett. **94**, 095701 (2005).
- [63] S. A. Shevlin, A. J. Fisher, and E. Hernandez, Phys. Rev. B **63**, 195306 (2001).
- [64] R. Ramírez, C. P. Herrero, E. R. Hernández, and M. Cardona, Phys. Rev. B **77**, 045210 (2008).
- [65] R. Martonák, L. Colombo, C. Molteni, and M. Parrinello, J. Chem. Phys. **117**, 11329 (2002).
- [66] P. Alippi, L. Colombo, P. Ruggerone, A. Sieck, G. Seifert, and T. Frauenheim, Phys. Rev. B **64**, 075207 (2001).
- [67] M. Cogoni, B. Uberuaga, A. Voter, and L. Colombo, Phys. Rev. B **71**, 121203 (2005).
- [68] R. Ramírez and C. P. Herrero, Phys. Rev. B **95**, 045423 (2017).
- [69] J.-B. Fournier and C. Barbetta, Phys. Rev. Lett. **100**, 078103 (2008).
- [70] H. Shiba, H. Noguchi, and J.-B. Fournier, Soft Matter **12**, 2373 (2016).
- [71] G. J. Martyna, M. E. Tuckerman, D. J. Tobias, and M. L. Klein, Mol. Phys. **87**, 1117 (1996).
- [72] R. Ramírez and C. P. Herrero, Phys. Rev. B **101**, 235436 (2020).
- [73] M. E. Tuckerman, *Statistical Mechanics: Theory and Molecular Simulation* (Oxford University Press, Oxford, 2010).
- [74] M. F. Herman, E. J. Bruskin, and B. J. Berne, J. Chem. Phys. **76**, 5150 (1982).
- [75] C. P. Herrero, R. Ramírez, and G. Herrero-Saboya, Phys. Rev. B **109**, 104112 (2024).
- [76] H. Sahin, S. Cahangirov, M. Topsakal, E. Bekaroglu, E. Akturk, R. T. Senger, and S. Ciraci, Phys. Rev. B **80**, 155453 (2009).
- [77] E. Scalise, M. Houssa, G. Pourtois, B. van den Broek, V. Afanas'ev, and A. Stesmans, Nano Res. **6**, 19 (2013).
- [78] X. Zhang, H. Xie, M. Hu, H. Bao, S. Yue, G. Qin, and G. Su, Phys. Rev. B **89**, 054310 (2014).
- [79] R. Ramírez and M. C. Böhm, Inter. J. Quantum Chem. **30**, 391 (1986).
- [80] A. Togo, L. Chaput, T. Tadano, and I. Tanaka, J. Phys.: Condens. Matter **35**, 353001 (2023).
- [81] L. Wirtz and A. Rubio, Solid State Commun. **131**, 141 (2004).
- [82] N. Mounet and N. Marzari, Phys. Rev. B **71**, 205214 (2005).
- [83] J.-A. Yan, W. Y. Ruan, and M. Y. Chou, Phys. Rev. B **77**, 125401 (2008).
- [84] R. Ramírez and C. P. Herrero, J. Chem. Phys. **151**, 224107 (2019).
- [85] R. Ramírez, C. P. Herrero, and E. R. Hernández, Phys. Rev. B **73**, 245202 (2006).
- [86] J. C. Garcia, D. B. de Lima, L. V. C. Assali, and J. F. Justo, J. Phys. Chem. C **115**, 13242 (2011).
- [87] D. Kaltsas, L. Tsetseris, and A. Dimoulas, Appl. Surf. Sci. **291**, 93 (2014).
- [88] C. Kittel, *Introduction to Solid State Physics* (Wiley, New York, 2005), 8th ed.
- [89] C. P. Herrero and R. Ramírez, Chem. Phys. **533**, 110737 (2020).
- [90] C. P. Herrero and R. Ramírez, Eur. Phys. J. B **96**, 147 (2023).
- [91] W. Gao and R. Huang, J. Mech. Phys. Solids **66**, 42 (2014).
- [92] L. Masson and G. Prevot, Nanoscale Adv. **5**, 1574 (2023).
- [93] F. Behroozi, Langmuir **12**, 2289 (1996).
- [94] L. D. Landau and E. M. Lifshitz, *Statistical Physics* (Pergamon, Oxford, 1980), 3rd ed.
- [95] H. B. Callen, *Thermodynamics and an Introduction to Thermostatistics* (John Wiley, New York, 1985).
- [96] R. S. Berny, S. A. Rice, and J. Ross, *Physical Chemistry* (Oxford University Press, New York, 2000).
- [97] A. Politano, A. R. Marino, D. Campi, D. Farías, R. Miranda, and G. Chiarello, Carbon **50**, 4903 (2012).
- [98] A. Politano and G. Chiarello, Nano Res. **8**, 1847 (2015).